Structure and grain growth of TiO$_2$ nanoparticles investigated by electron and x-ray diffractions and ^{181}Ta perturbed angular correlations

S. Schlabach,[a)] D. V. Szabó, and D. Vollath[b)]
*Institut für Materialforschung III, Forschungszentrum Karlsruhe GmbH, P.O. Box 3640,
D-76021 Karlsruhe, Germany*

P. de la Presa and M. Forker
*Helmholtz Institut für Strahlen- und Kernphysik, University of Bonn, Nussallee 14-16,
D-53115 Bonn, Germany*

Bare and coated TiO$_2$ nanoparticles with particle sizes $d < 5$ nm have been synthesized in a microwave plasma process. Structural properties of these materials have been investigated by transmission electron microscopy, x-ray diffraction, and perturbed angular correlation (PAC) measurements of the electric quadrupole interaction (QI) at the probe nucleus ^{181}Ta on the metal site of TiO$_2$ at temperatures $290 \leq T \leq 1450$ K. The electron diffraction of the uncoated nanoparticles in the as-synthesized state reflects long range order in the Ti sublattice. Depending on the particles size, either the anatase or the rutile phase of TiO$_2$ was found. Anatase appears to be the stable form of nanocrystalline TiO$_2$ below $d \sim 10$ nm. The PAC spectra of these nanocrystalline oxides are characterized by a broad distribution of strong quadrupole interactions, indicating a strongly disordered oxygen environment of the metal sites. Upon annealing, the grain size grows from $d < 5$ nm after synthesis to $d > 100$ nm after 1300 K. PAC spectra taken in the same temperature range show that with increasing temperature, the initially disordered state transforms to well-ordered rutile TiO$_2$. The data suggest a critical grain size of $d \sim 10$ nm for the onset of the ordering process. The spectra of coarse-grained TiO$_2$ are reached at a particle size $d \gtrsim 30$ nm. In n-TiO$_2$ coated with Al$_2$O$_3$ and ZrO$_2$ both the cores and the coatings were found to grow with increasing temperature; the cores of the coated particles, however, grow much less than those of the noncoated particles. The PAC method was used to investigate the QI in both TiO$_2$ cores and in the ZrO$_2$ coating of n-TiO$_2$/ZrO$_2$ at different temperatures. These data suggest that although the coated particles grow with temperature, the ordering process is obstructed, possibly by a solid state reaction between the TiO$_2$ kernels and the coatings. © *2006 American Institute of Physics.* [DOI: 10.1063/1.2214182]

I. INTRODUCTION

Titania (TiO$_2$) is a wide band gap (~ 3.2 eV) semiconductor with interesting optoelectronic and photochemical properties. The photocatalytic ability is influenced by its phase structure and particle size.[1] TiO$_2$ is often reported to occur in the metastable anatase rather than the stable rutile structure when its size is in the nanometer range [e.g., Refs. 2–4]. This observation is usually attributed to the difference in surface free energies of possible phases [e.g., Refs. 5–7]. The importance of this difference increases with decreasing particle size, leading to a different phase stability in the nanometer range compared to the coarse-grained (cg) material [e.g., Refs. 5–7]. The occurrence of anatase is interesting in several technological applications because it is more efficient in catalysis, photocatalysis, and solar cells than the coarse-grained stable rutile phase.[6] Therefore it is of great importance to understand in detail the structure, phase transformations, and grain growth in nanoscaled TiO$_2$.

In this paper an investigation of structural properties of nanocrystalline (n-) TiO$_2$ synthesized as bare and coated par-

ticles using the microwave plasma process[8,9] is presented. The starting material consists of very small particles with diameter $d < 5$ nm. Typically, powders synthesized with the microwave plasma process show a narrow particle size distribution.[10]

For the investigation standard analytical methods of the material sciences such as transmission electron microscopy (TEM) and x-ray diffraction (XRD) are combined with perturbed angular correlation (PAC) spectroscopy, which is a well-established technique for the investigation of hyperfine interactions.[11,12] Here, PAC spectroscopy is used to study the electric quadrupole interaction (QI) between the nuclear electric quadrupole moment Q of a probe nucleus and the tensor of the electric-field gradient (EFG) at the nuclear site. The EFG is determined by the charge distribution surrounding the probe nucleus. Because of its r^{-3} dependence, the major contribution to the QI comes from the nearest-neighbor charges. PAC therefore gives information on the short range order, whereas TEM and XRD are mainly used to investigate long range order. For these reasons the different methods have been used to get complementary insights into structure evolution, phase transition, and grain growth in nanocrystalline (n-) TiO$_2$ particles as a function of heat treatment.

a)Electronic mail: sabine.schlabach@imf.fzk.de
b)Present address: NanoConsulting, Primelweg 3, D-76297 Stutensee, Germany.

100, 024305-1

TABLE I. Results of the electron and x-ray diffraction studies of TiO_2 nanoparticles.

Compound	Precursor	Structure and diameter d^a		
		TEM as synthesized	XRD as synthesized	XRD after 1273 K
Ti(Hf)O$_2$ (Sample I)	Butoxide	Anatase/(rutile) $d \sim 2$–8 nm	Mainly amorphous, some anatase (rutile?)	Rutile—$d > 100$nm^b annealing see Fig. 3
Ti(Hf)O$_2$ (Sample II)	Butoxide	Anatase/(rutile), $d \sim 2$ nm	Mainly amorphous, some anatase (rutile?)	Rutile—$d > 90$ nm^b annealing see Fig. 3
Ti(Hf)O$_2$/Al$_2$O$_3$	Butoxide/chloride		Anatase, rutile	Rutile—$d \sim 31$ nm, corundum—$d \sim 43$ nm
Ti(Hf)O$_2$/ZrO$_2$ (Sample I)	Butoxide/butoxide	c/t-ZrO$_2$, ~ 5 nm	c/t-ZrO$_2$—$d \sim 5$ nm, rutile—$d \sim 6$ nm	c/t-ZrO$_2$—$d \sim 20$ nm, m-ZrO$_2$—$d \sim 30$ nm
Ti(Hf)O$_2$/ZrO$_2$ (Sample II)	Butoxide/chloride	c/t-ZrO$_2$, possibly some anatase	Mainly c/t-ZrO$_2$—$d \sim 6$ nm, possibly some anatase, rutile	
TiO$_2$/Zr(Hf)O$_2$	Chloride/chloride		Anatase—$d \sim 8$ nm, rutile—$d \sim 8$ nm, c/t-ZrO$_2$, possibly some m-ZrO$_2$	c/t-ZrO$_2$—$d \sim 20$ nm, rutile—$d \sim 49$ nm, maybe some ZrTiO$_4$

$^a d$ determined using Scherrer formula (see Ref. 18).
^{b}Diameter d is only a rough estimation since $\beta_{net}^{1/2} \sim \beta_{instr}^{1/2}$.

For the application of PAC spectroscopy, suitable radioactive probe nuclei have to be introduced into the compounds of interest. Among the most favorable PAC radioisotopes are [181]Hf and [111]Cd. The β decay of [181]Hf ($T_{1/2} = 45$ d) populates the excited states of [181]Ta, and the EC decay of [111]In ($T_{1/2} = 2.8$ d) those of [111]Cd. In TiO$_2$, both probes occupy the substitutional Ti site. This has been concluded from PAC measurements of the QI in coarse-grained polycrystalline TiO$_2$ (Ref. 13) and in TiO$_2$ single crystals.[14,15] For the present investigation of nanocrystalline n-TiO$_2$, we have chosen [181]Hf/[181]Ta as probe nucleus for reasons discussed in Sec. III.

In the course of this study, bare and coated TiO$_2$ nanoparticles doped with 4 at. % of stable Hf were synthesized [n-Ti(Hf)O$_2$]. Coatings of amorphous Al$_2$O$_3$ and crystalline ZrO$_2$ were produced. The nonradioactive particles were characterized by XRD and TEM at room temperature in the as-synthesized state and in most cases also after a high-temperature treatment. In case of the bare nanoparticles, the temperature induced changes of structure and particle size were investigated by a detailed annealing program. With the PAC measurements, the QI of the neutron-irradiated nanoparticles was studied as a function of temperature in the range of $77 \leqslant T \leqslant 1500$ K. In the case of ZrO$_2$-coated particles, the QI in the TiO$_2$ core and in the ZrO$_2$ coating was investigated separately. For these PAC measurements, particles with a Hf-doped TiO$_2$ core and a Hf-free ZrO$_2$ coating [n-Ti(Hf)O$_2$/ZrO$_2$] and particles with a Hf-free TiO$_2$ core and a Hf-doped ZrO$_2$ coating [n-TiO$_2$/Zr(Hf)O$_2$] were synthesized and neutron irradiated.

The present work is the extension of a previous study in which TEM, XRD, and PAC were combined to characterize phases and identify phase transitions of nanocrystalline n-ZrO$_2$.[16,17]

II. SAMPLE PREPARATION AND CHARACTERIZATION BY TEM AND XRD

A. Powder synthesis

Nanosized TiO$_2$ (n-TiO$_2$) samples were synthesized by the Karlsruhe microwave plasma process (KMPP). This gas phase process allows the preparation of bare and coated particles with a narrow particle size distribution.[10] As precursors butoxides [Ti-t-butoxide, Ti(OC$_4$H$_9$)$_4$; Hf-t-butoxide, Hf(OC$_4$H$_9$)$_4$; and Zr-t-butoxide, Zr(OC$_4$H$_9$)$_4$] and chlorides (TiCl$_4$, HfCl$_4$, and ZrCl$_4$) were used (Table I). In the process the water-free precursors were evaporated and transformed to oxides using a microwave plasma discharge and an Ar/20 vol % O$_2$ gas mixture as reaction gas. The coating of single particles was realized by using two plasma stages consecutively. The working pressure was in the range of 5–10 mbars, the temperature in the plasma zones was <900 K. The Hf-doping was performed by adding appropriate amounts of the corresponding Hf precursors.

B. TEM and XRD measurements

For electron microscopic studies a Philips (CM-30 ST) transmission electron microscope (TEM) was used for recording electron diffraction and microscopic patterns. The samples were prepared on copper grids covered with a holey carbon film by dipping a grid into the powder. X-ray measurements (XRD) were done with a Philips (X'Pert) diffractometer. The diffraction data were recorded with Cu $K\alpha$ radiation. To study grain growth and structure changes with increasing temperature, selected powders were annealed at 473, 673, 873, and 1073 K for 6 h and at 1273 K for 20 h, respectively, in ambient air. X-ray diffraction was carried out afterwards at room temperature on noncompacted powder samples. The Scherrer formula[18] is used to determine the crystal size using the linewidth of the XRD spectra after correction for instrumental broadening. To get the net line-
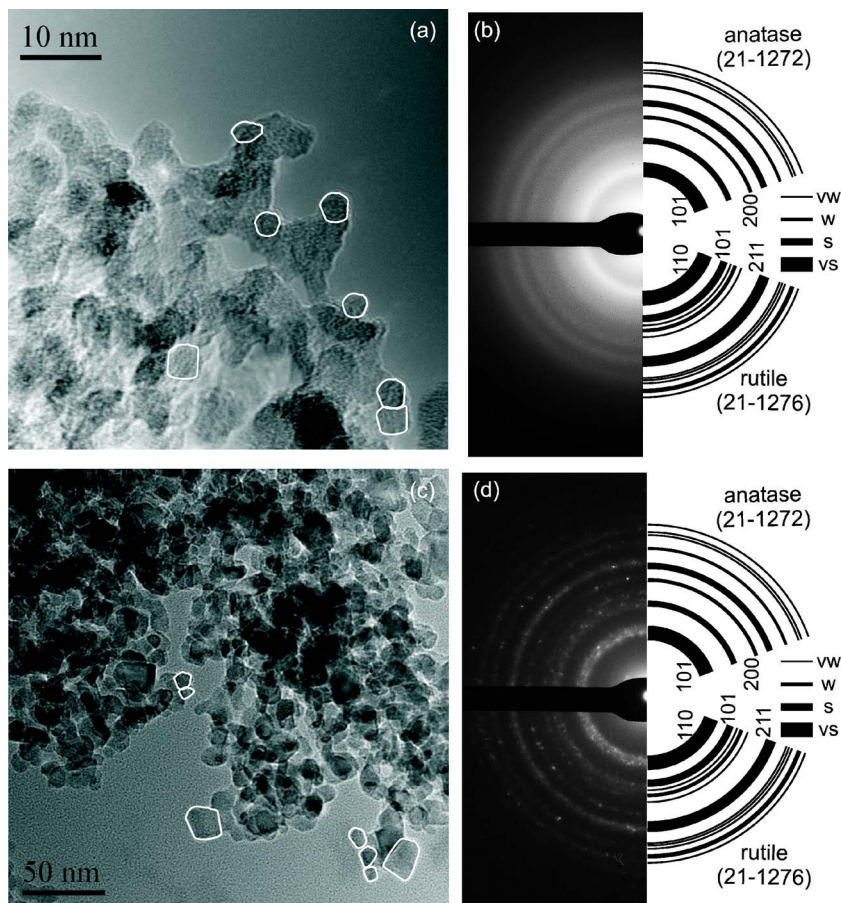
FIG. 1. TEM micrograph and electron diffraction pattern of n-TiO$_2$ of the as-synthesized state [(a) and (b)] and after heat treatment for 6 h at 873 K [(c) and (d)], respectively. For clarification some particles are highlighted in the electron micrographs [(a) and (c)]. The right-hand sections of (b) and (d) show the reference electron diffraction patterns of the anatase (JCPDS 21-1272, top) and rutile (JCPDS 21-1276, bottom) structures (see Ref. 19). The line width of the corresponding anatase and rutile references represents the intensity of the hkl reflections; very strong (vs), strong (s), weak (w), and very weak (vw).

width $\beta_{\text{net}}^{1/2}$ Eq. (1) is applied to the measured linewidth $\beta_{\text{exp}}^{1/2}$ determining the instrumental broadening $\beta_{\text{instr}}^{1/2}$ using LaB$_6$ microcrystals,

$$\beta_{\text{net}}^{1/2} = \sqrt{(\beta_{\text{exp}}^{1/2})^2 - (\beta_{\text{instr}}^{1/2})^2}. \tag{1}$$

For crystal sizes larger than $\sim$100 nm Eq. (1) is only a rough estimation since $\beta_{\text{exp}}^{1/2}$ is then similar to $\beta_{\text{instr}}^{1/2}$.

C. Results

1. Uncoated n-TiO₂ particles

The main results of the TEM and XRD measurements are collected in Figs. 1–4 and Table I. Figure 1 shows an electron micrograph [Fig. 1(a)] and an electron diffraction pattern [Fig. 1(b)] of bare n-Ti(Hf)O$_2$ powder in the as-synthesized state. The right-hand section of Fig. 1(b) illustrates the reference electron diffraction patterns of anatase [JCPDS (Ref. 19) 21-1272, top] and rutile [JCPDS (Ref. 19) 21-1276, bottom], respectively. The micrograph reflects a rather narrow distribution of particle sizes around 2–5 nm. The analysis of the electron diffraction pattern indicates a predominance of the anatase structure of the as-synthesized TiO$_2$ nanoparticles. Minor contributions of the rutile phase cannot be excluded. The anatase phase has also been found in a recent study of n-TiO$_2$ prepared by chemical vapor deposition.[20] An evaluation of the linewidth leads to a particle size of about 2 nm matching the results of the electron micrograph.

The XRD pattern of bare n-TiO$_2$ (bottom most spectrum in Fig. 2) consists only of a broad shoulder at $2\Theta \sim 25°$ and

therefore yields no information on the structure of the TiO$_2$ nanoparticles. The width of this shoulder indicates extremely small ($d \leq 5$ nm) and possibly amorphous particles. The mechanism responsible for the remarkable differences between the XRD and the electron diffraction pattern, i.e., several well defined rings versus one broad shoulder, is presently not clearly identified. In this context one should keep in mind that a single electron diffraction pattern is not necessarily representative for the entire sample, since it only reflects the degree of crystalline order of the small area hit by the electron beam. A similar difference between electron diffraction and XRD patterns has been observed, e.g., for cold rolled NiTi shape memory alloys.[21]
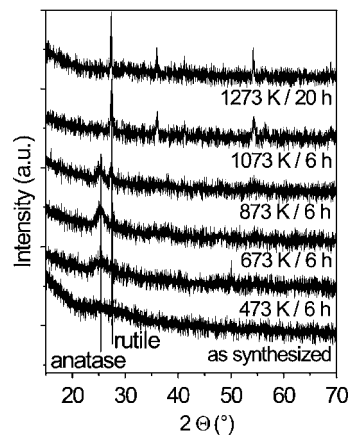

FIG. 2. Room temperature x-ray diffraction spectra of n-Ti(Hf)O$_2$ (sample II) after annealing in air for 6–20 h at the given temperatures.
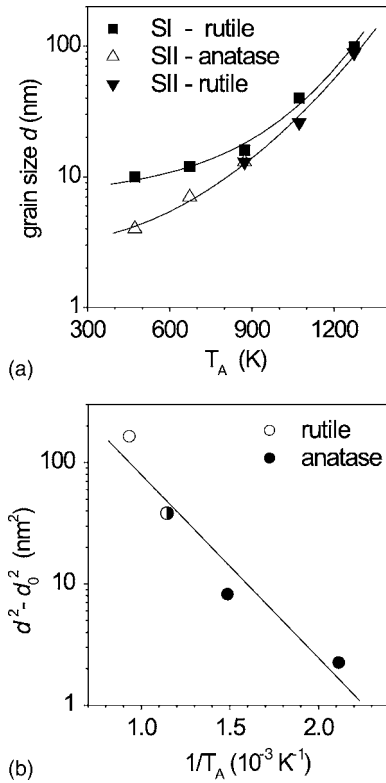
FIG. 3. (a) Size of *n*-TiO$_2$ particles (samples I and II) as a function of the annealing temperature T_A. The crystal size determined by Scherrer formula (see Ref. 18) at $T \sim 1200$ K is only a rough estimation since the determined net peak width $\beta_{net}^{1/2}$ in XRD is close to the instrumental broadening $\beta_{instr.}^{1/2}$. (b) Arrhenius plot for the determination of the grain growth enthalpy Q_A. Data points are restricted to sample II and those with a dwell time of 6 h. The grain growth exponent is assumed to be 2 according to the most probable gas phase diffusion process.

The changes of structure and size of bare *n*-TiO$_2$ particles caused by annealing at higher temperatures are illustrated in Figs. 1(c) and 1(d) and by the other XRD spectra in Fig. 2. The anatase structure, which is the first to emerge from the broad shoulder at $2\Theta \sim 25°$, is stable up to annealing temperatures of $T \sim 900$ K where the crystal size reaches $d \sim 13$ nm [see Fig. 3(a)]. This is in good agreement with the thermodynamic analysis of the phase stability of *n*-TiO$_2$ by Zhang and Banfield.[22] Our result also agrees with the experimental findings of Ghosh *et al.*[6] for *n*-TiO$_2$ prepared by combustion flame chemical vapor deposition where the transition to the rutile phase sets in at $T > 870$ K at an anatase particle size of $d \sim 13.5$ nm. At $T > 670$ K, rutile lines appear in the XRD spectra at the expense of the anatase reflections, and after annealing at $T \sim 1000$ K the particles are crystallized in the rutile phase. The particle size estimated from the width of the diffraction lines using the Scherrer formula is shown in Fig. 3(a) as a function of the annealing temperature for two samples of bare TiO$_2$ nanoparticles. Substantial crystal growth sets in at $T \sim 900$ K. In both samples, the crystal size reaches $d > 100$ nm after annealing at 1300 K. Assuming normal grain growth, the grain growth equation (e.g., Ref. 23) can be used for an estimation of the activation energy. The grain growth exponent determining the grain growth process is supposed to be 2 according to the most probable gas phase diffusion process. Using an Arrhenius plot [Fig.
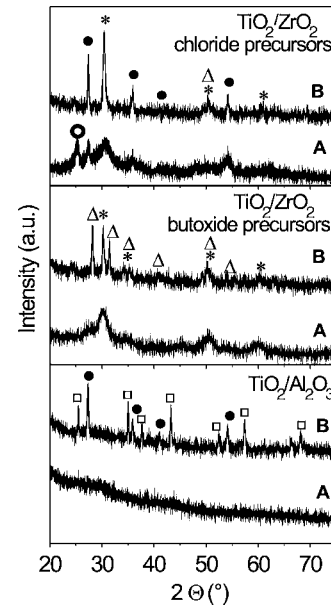

FIG. 4. Room temperature x-ray diffraction spectra of coated *n*-TiO$_2$ particles after synthesis (A) and after annealing in air for 20 h at 1273 K (B). The following symbols are used to mark the reflections of the different compounds involved: (●) rutile TiO$_2$, (○) anatase TiO$_2$, (∗) cubic/tetragonal ZrO$_2$, (△) monoclinic ZrO$_2$, and (□) corundum Al$_2$O$_3$ (see Ref. 19).

3(b)], the grain growth activation enthalpy is then estimated to be $Q_A \sim 30$ kJ/mol, which is in the same order as the Q_A values of nanocrystalline TiO$_2$ synthesized by gas phase condensation[24] [$Q_A = 83(40)$ kJ/mol] and combustion flame chemical vapor deposition[6] [$Q_A = 63(10)$ kJ/mol for rutile at $T > 873$ K]. The likeness in the Q_A values suggests a considerable structural similarity of materials synthesized by entirely different methods.

2. Coated n-TiO$_2$ particles

XRD spectra of *n*-TiO$_2$ particles coated with Al$_2$O$_3$ or ZrO$_2$ are shown in Fig. 4 for the as-synthesized state and after annealing in air for 20 h at 1273 K. According to these spectra, in the as-synthesized state, the coating consists of amorphous Al$_2$O$_3$ or cubic/tetragonal (*c/t*-) ZrO$_2$ (see the XRD patterns A in Fig. 4). After annealing at 1273 K, the XRD spectrum of *n*-Ti(Hf)O$_2$/Al$_2$O$_3$ shows the reflections of rutile and corundum, with the linewidths corresponding to particles sizes of 31 and 43 nm, respectively (see Table I). Obviously, the titania kernels exhibit an appreciable grain growth in spite of the coating. The coating reduces the rate of grain growth significantly; it does, however, not act as perfect diffusion barrier. Possibly, a local formation of structural Al$_2$TiO$_5$ elements enables the Ti^{4+} ions to pass the alumina barrier. In the PAC spectra of these particles, a weak QI with $\nu_q \sim 260(10)$ MHz appears at $T \geqslant 1100$ K (see Sec. III C). Possibly, this component reflects the formation of intermediary Al$_2$TiO$_5$.

Two XRD spectra of ZrO$_2$-coated titania nanoparticles are shown in Fig. 4. The topmost spectrum refers to *n*-TiO$_2$/Zr(Hf)O$_2$ prepared from chloride precursors. After annealing, above 1300 K, one finds the diffraction lines of *c/t*-ZrO$_2$ and—in spite of the much larger x-ray scattering

cross section of Zr—those of rutile TiO_2 corresponding to a particle of size $d \sim 50$ nm. In the case of n-Ti(Hf)O_2/ZrO_2 prepared from butoxide precursors (center spectrum in Fig. 4), only the diffraction lines of c/t- and m-ZrO_2 were observed.

The observation of rutile lines in the topmost spectrum [note that these coincide exactly with those of bare rutile (Fig. 2) and are incompatible with a contribution of textured m-ZrO_2] and their absence in the center spectrum might be seen as indications that only the particles prepared from butoxide precursors (center spectrum) are homogeneously covered with a ZrO_2 coating such that the reflections of the TiO_2 core are completely suppressed.

The XRD measurements (Fig. 4) thus show that both the cores and the coatings of the coated n-TiO_2 nanoparticles grow with increasing temperature. Growth of the coatings during annealing is only possible by sintering of the particles, although the powders were not compacted. The kernel of the coated grains grows less than that of the noncoated particles under similar annealing conditions. The core of all coated TiO_2 nanoparticles, however, reaches a size of $d \geqslant 30$ nm after heating to 1273 K.

III. PAC MEASUREMENTS

A. Experimental details

One argument favoring ^{181}Hf/^{181}Ta over ^{111}In/^{111}Cd for a PAC study of nanocrystalline TiO_2 comes from sample preparation aspects. ^{181}Hf is usually produced by thermal neutron activation of stable ^{180}Hf (natural abundance of 18.5 at. %). As thermal neutron irradiation of stable Ti leads only to short-lived radioactivity (^{51}Ti, $T_{1/2}$=5.6 min), the PAC probe ^{181}Hf can be introduced by first doping n-TiO_2 with stable Hf during the synthesis and then neutron irradiating the doped nanoparticles enclosed, e.g., in a quartz tube. This avoids handling open radioactivity in the sample preparation, which is clearly a very important advantage when dealing with a noncompacted powder of nanoparticles. In the case of ^{111}Cd, it would be difficult to avoid handling of radioactive nanoparticles because the radioisotope would have to be introduced either during or after the synthesis. Other advantages of ^{181}Hf/^{181}Ta over ^{111}Cd/^{111}In are the much longer half-life of the mother isotope, which allows running extensive temperature programs with the same sample, and the fact that Hf and Ti have both valence 4+.

For the production of the PAC sources, noncompacted powder of Hf-doped n-TiO_2 (typically a few mg) was enclosed under vacuum into quartz tubes and irradiated in a flux of thermal neutrons of 5×10^{13} n/s cm^2 for times of the order of 24 h. The samples were mounted in a furnace designed for temperatures up to 2300 K.[25] The PAC spectra of the 133–482 keV cascade of ^{181}Ta were measured as a function of temperature in the range of $290 \leqslant T \leqslant 1500$ K. In most cases, the sample temperature was raised in steps of 50–100 K and after reaching 1500 K, decreased in similar steps back to room temperature. The spectra were taken with a standard four-detector setup equipped with fast BaF_2 scintillators. Their truncated conical shape allows a minimum sample-detector distance of 11 mm.[25]

B. Data analysis

The static quadrupole interaction between the electric quadrupole moment Q of a nuclear state and the electric-field gradient acting at the nuclear site is usually described by two independent parameters, the quadrupole frequency $\nu_q = eQV_{zz}/h$ and the asymmetry parameter $\eta = (V_{xx} - V_{yy})/V_{zz}$, where $V_{ii} = \delta^2 V/\delta_{ii}^2$ ($i=x,y,z$) are the principal-axis components of the EFG tensor with $|V_{xx}| \leqslant |V_{yy}| \leqslant |V_{zz}|$.

These parameters can be derived from the PAC spectra. Hyperfine interactions lead to a time modulation of the angular correlation coefficients A_{kk}, ($k=2,4$) of a cascade of two successive γ rays. In the case of a perturbation by static hyperfine interactions in polycrystalline samples, the modulation can be expressed by the perturbation factor $G_{kk}(t)$ (for details see, e.g., Refs. 11 and 12),

$$G_{kk}(t) = s_{k0} + \sum_n s_{kn} \cos(\omega_n t) \exp\left(-\tfrac{1}{2}\delta\omega_n t\right). \quad (2)$$

The frequencies ω_n in this sum of oscillatory terms are associated with the energy differences between the hyperfine levels into which the nuclear state is split by the hyperfine interaction. In the present case of a static QI, the frequencies ω_n depend on the quadrupole frequency ν_q and on the asymmetry parameter η. The amplitudes are functions of η only.

The exponential factor in Eq. (2) accounts for possible distributions of the static hyperfine interaction caused by structural, chemical, and other defects. In this case, the nuclear spins of the ensemble no longer precess all with the same frequency and an attenuation of the oscillation amplitudes results, which is the stronger the broader the distribution. The parameter δ in Eq. (2) is the relative width of a Lorentzian distribution.

Frequently, several fractions of nuclei subject to different hyperfine interactions are found in the same sample. The effective perturbation factor is then given by

$$G_{kk}(t) = \sum_i f_i G_{kk}^i(t), \quad (3)$$

where f_i (with $\Sigma_i f_i = 1$) is the relative intensity of the ith fraction.

For γ-γ cascades with vanishing angular correlation coefficient A_{44}, the perturbation factor $G_{22}(t)$ can be determined by taking the coincidence spectra $N(\Theta,t)$ at angles $\Theta = 90°$ and $180°$ between two detectors:

$$A_{22}^{\exp} \sum_i f_i G_{22}^i(t) = 2[N(180,t) - N(90,t)]/[N(180,t)$$

$$+ 2N(90,t)]. \quad (4)$$

[Note that the finite solid angle integration attenuates the coefficient A_{44} much stronger than the coefficient A_{22}. The 133–482 keV cascade of ^{181}Ta has a coefficient $A_{44} \sim 0.07$. The large solid angle of our setup, however, leads to $A_{44}^{\exp} \approx 0.0$, which justifies the neglect of the A_{44} term in Eq. (4).]

In the experiment, the anisotropy coefficient A_{22} of the γ-γ cascade is modified by the experimental conditions, such as the finite solid angle extended by the detectors, the time resolution relative to the precession period, eventual prompt coincidences, and other factors. As shown by Eq. (4), exact
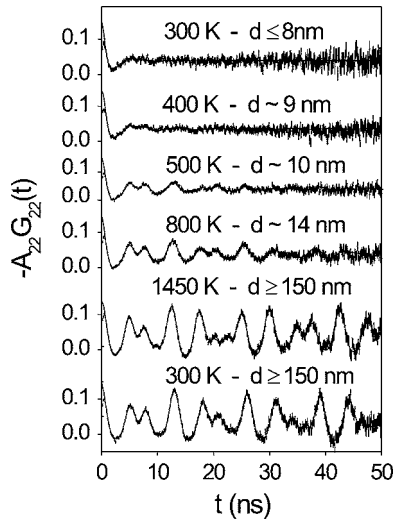
FIG. 5. ^{181}Ta PAC spectra of noncoated n-Ti(Hf)O$_2$ (sample I) at different temperatures. The particle sizes d at a given temperature correspond to those shown in Fig. 3.

FIG. 6. The rutile fraction and the relative linewidth δ of the quadrupole frequency of two samples (I and II) of noncoated n-Ti(Hf)O$_2$ nanoparticles as a function of temperature. The insert shows the linewidth as a function of the particle size (sample I, Fig. 3).

knowledge of the experimental anisotropy A_{22}^{exp} is required for a precise determination of the relative amplitudes f_i of the fractions with different hyperfine interactions present in the same sample. For an experimental determination of A_{22}^{exp} of our setup, we have measured the ^{181}Ta angular correlation of HfOCl$_2$ dissolved in dilute HCl for different source detector distances. In a liquid source of HfOCl$_2$, the time average of the rapidly fluctuating QI almost vanishes and the anisotropy therefore decreases only very slowly with increasing time.[26] In a semilogarithmic plot of the anisotropy versus time, one obtains a straight line corresponding to a decay constant $\lambda_2 \approx 85$ MHz. By extrapolation to $t=0$, the experimental anisotropy A_{22}^{exp} of the setup can be determined with a precision of the order of 5%. In the analysis of the n-TiO$_2$ spectra, the value of A_{22}^{exp} for the given sample-detector separation of the measurement was then treated as fixed parameter.

C. Results

Two samples of noncoated n-Ti(Hf)O$_2$ nanoparticles have been studied by PAC spectroscopy. Figure 5 illustrates the typical evolution of the ^{181}Ta PAC spectra with increasing temperature using the data of sample I. The particle sizes included in Fig. 5 have been determined from the room temperature XRD spectra of the same, nonradioactive sample after annealing at the given temperatures (see sample I in Fig. 2).

After synthesis at 300 K, the PAC spectra of both samples show the typical features of a perturbation by a broad distribution of strong, static QIs, i.e., a fast initial decay of the anisotropy and a constant ("hard core," Refs. 11 and 12) value at larger delay times practically without any oscillatory structure. A fit of Eq. (2) to the 300 K spectrum in Fig. 5 leads to a quadrupole frequency $\nu_q=900(50)$ MHz, an asymmetry parameter $\eta=0.48(5)$, and a relative width $\delta =0.60(5)$ of the Lorentzian frequency distribution.

In sample I, an oscillatory structure starts to appear at $T \sim 500$ K and in sample II at $T \sim 800$ K. With further in-
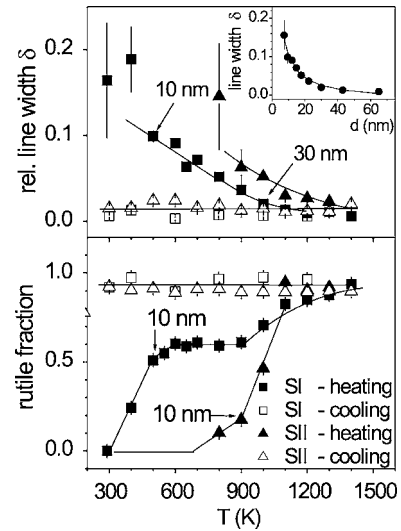
crease of temperature, the oscillation amplitudes grow and at $T \sim 1400$ K the PAC spectra of ^{181}Ta in the two samples n-Ti(Hf)O$_2$ have become identical to that of ^{181}Ta in coarse-grained rutile TiO$_2$.[13] From 500 K (sample I) or 800 K (sample II) onwards, two components or fractions are necessary to describe the PAC spectra, one characterized by the broad frequency found after the synthesis ("disordered" fraction) and the other subjected to a sharper QI, which gives rise to the visible oscillations. With increasing temperature, the QI parameters of the latter component evolve towards those of ^{181}Ta in coarse-grained rutile TiO$_2$.[13] This fraction will therefore be denominated as "rutile" fraction. The main results of the analysis are collected in Figs. 6 and 7. The full and open symbols in these figures describe the changes of the parameters caused by heating from 300 to 1400 K and subsequent cooling back to room temperature, respectively. The lower section of Fig. 6 shows the relative intensity of the rutile fraction of samples I and II of bare n-Ti(Hf)O$_2$, the upper section the relative linewidth of the QI of the rutile fraction. Again, the crystal sizes derived from the XRD spec-
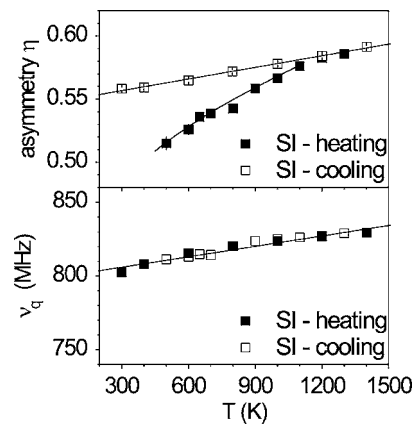

FIG. 7. The quadruple frequency ν_q and the asymmetry parameter η of ^{181}Ta in noncoated n-Ti(Hf)O$_2$ nanoparticles as a function of temperature.
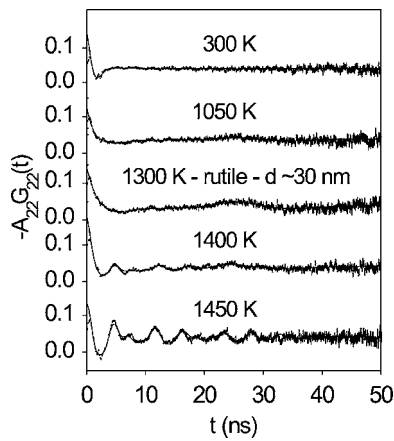
FIG. 8. ^{181}Ta PAC spectra of Al$_2$O$_3$-coated Hf-doped TiO$_2$ nanoparticles—n-Ti(Hf)O$_2$/Al$_2$O$_3$.

tra of the annealed nonirradiated samples I and II (Figs. 2 and 3) are included. The quadrupole frequency ν_q and the asymmetry parameter η of sample I are displayed in Fig. 7 as a function of temperature. $\nu_q(T)$ and $\eta(T)$ of sample II coincide with the trends found with sample I. Within relatively wide error bands, the QI parameters of the disordered fraction presented no pronounced temperature dependence.

The main results of the PAC study of the coated TiO$_2$ nanoparticles are illustrated in Figs. 8 and 9. Figure 8 shows the PAC spectra of ^{181}Ta in the TiO$_2$ core of Al$_2$O$_3$-coated
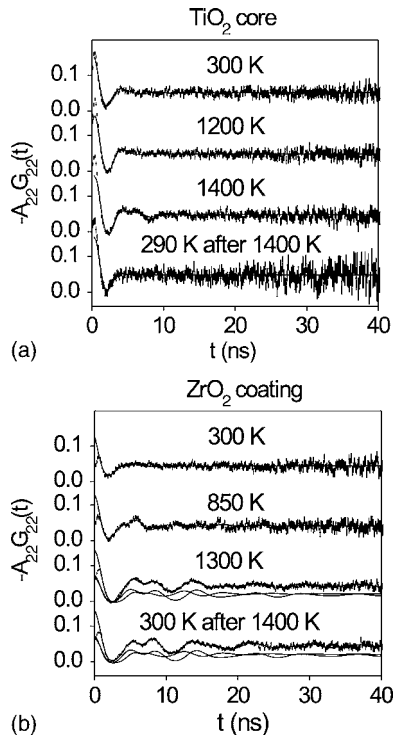

(a)

(b)

FIG. 9. ^{181}Ta PAC spectra of ZrO$_2$-coated n-TiO$_2$ nanoparticles. The topmost and bottommost series show the spectra of the TiO$_2$ core and the ZrO$_2$ coating, respectively. They were obtained from particles with Hf-doped TiO$_2$ core and nondoped coating [n-Ti(Hf)O$_2$/ZrO$_2$] and particles with Hf-doped ZrO$_2$-coating and nondoped TiO$_2$-core [n-TiO$_2$/Zr(Hf)O$_2$], respectively. The solid and the dotted lines in the spectra of n-TiO$_2$/Zr(Hf)O$_2$ at 1300 K correspond approximately to the PAC pattern of monoclinic and tetragonal ZrO$_2$, respectively.

particles [n-Ti(Hf)O$_2$/Al$_2$O$_3$]; Fig. 9 presents the spectra measured in n-TiO$_2$ nanoparticles coated with ZrO$_2$. The topmost series in Fig. 9 shows the spectra of ^{181}Ta in the TiO$_2$ core [n-Ti(Hf)O$_2$/ZrO$_2$, sample I in Table I, prepared from butoxide/butoxide precursors], the bottommost series those of ^{181}Ta in the ZrO$_2$ coating [n-TiO$_2$/Zr(Hf)O$_2$, prepared from chloride/chloride precursors]. The spectra of n-Ti(Hf)O$_2$/ZrO$_2$ prepared from butoxide/chloride precursors (sample II in Table I) agree in the main features with those prepared from butoxide/butoxide precursors (Fig. 9).

After synthesis, the spectra of all coated particles reflect a perturbation by a broad distribution of strong static QIs—just as those as the noncoated particles. In contrast to the bare particles, however, the spectra of the coated particles change only slightly with increasing temperature. The features of broad QI distributions, representative of a high degree of disorder, persist up to high temperatures. First indications of small-amplitude oscillations appear only at $T \geqslant 1300$ K. This is particularly true for the core of the coated particles (Fig. 8 and topmost series of Fig. 9). In the case of n-Ti(Hf)O$_2$/Al$_2$O$_3$, a first oscillation reflecting the onset of an order process is found at $T \sim 1100$ K. This component (relative intensity $\sim 20\%$ at 1300 K) represents a relatively weak, axially symmetric QI with frequency $\nu_q \sim 260(10)$ MHz and linewidth $\delta \sim 0.2$ and possibly reflects a solid state reaction between core and coating, leading to Al$_2$TiO$_5$. Heating to $T = 1450$ K is necessary to produce a large oscillatory PAC signal. The spectrum at 1450 K consists of two components (intensity ratio 3:1) with parameters $\nu_q = 920(15)$ MHz, $\eta = 0.79(3)$, and $\delta = 0.08(1)$ and $\nu_q = 920(10)$ MHz, $\eta = 0.59(2)$, and $\delta = 0.11(1)$ for the majority and the minority fractions, respectively. The parameters of the majority component are close to those of cg TiO$_2$ in this temperature range. The structure of the 1450 K spectrum is maintained when cooling down to room temperature.

For the core of ZrO$_2$-coated n-Ti(Hf)O$_2$ the broad frequency distribution persists to even higher temperatures (see spectra in Fig. 9). In this case, $T = 1400$ K is insufficient to induce an irreversible oscillatory structure in the PAC spectrum.

The ZrO$_2$ coating of n-TiO$_2$/Zr(Hf)O$_2$ shows a slightly different behavior (bottommost series in Fig. 9). Here, oscillations of small amplitude start to appear at $T \sim 800$ K. Two components are necessary to reproduce the spectra measured at $T \geqslant 1000$ K. The QI parameters of these components (intensity ratio 4:1) at 300 K after 1300 K are $\nu_q = 792(10)$ MHz, $\eta = 0.41(2)$, and $\delta = 0.18(1)$ and $\nu_q = 1180(20)$ MHz, $\eta = 0.31(3)$, and $\delta = 0.16(2)$ for the majority and minority fractions, respectively. These parameters are similar to those measured in the monoclinic (m) and the tetragonal (t) phase of zirconia nanoparticles[16] [m-ZrO$_2$: $\nu_q = 810(3)$ MHz, $\eta = 0.36(1)$, and $\delta = 0.08(1)$; t-ZrO$_2$: $\nu_q = 1260(13)$ MHz, $\eta = 0.13(1)$, and $\delta = 0.01(1)$], which suggests that after heating to 1400 K, the ZrO$_2$ coating of TiO$_2$/Zr(Hf)O$_2$ consists of a mixture of more or less well crystallized monoclinic and tetragonal ZrO$_2$. This interpretation is in agreement with the appearance of c/t- and m-ZrO$_2$ reflections in the XRD pattern of annealed n-TiO$_2$/Zr(Hf)O$_2$ (see Fig. 4).

IV. DISCUSSION

Taken together, the electron and x-ray diffraction data and the PAC results provide valuable information on the structure of the titania nanoparticles. The electron diffraction pattern clearly indicates long range ordering in the Ti cation sublattice. Both electron and x-ray diffractions show that n-TiO$_2$ particles synthesized in the microwave plasma process crystallize in the metastable anatase structure rather than in the stable rutile structure.

The observation of a broad frequency distribution in the PAC spectra indicates a high degree of disorder in the oxygen sublattice. Because of the r^{-3} dependence of the EFG, the measurements of the QI mainly sample the charge distribution of the nearest-neighbor environment of the probe. The nearest neighbors of a probe nucleus on a Ti site of crystalline TiO$_2$ are oxygen ions. The broad QI distribution found in the PAC spectra therefore implies a disorder of the nearest-neighbor oxygen environment of the probe nuclei.

This oxygen disorder cannot be attributed to the probes in the surface layer of the nanoparticles alone. Because of the r^{-3} dependence of the QI, surface effects probably go not beyond 0.5 nm. It is easy to estimate[27] that even if all probe nuclei within a 1 nm layer feel a surface-related disorder, not more than $\sim$50% of the probes would be affected at a particle size of 5 nm. The annealing experiments (see Sec. II) and PAC measurements, however, have established (see Fig. 6) that the particle size has to reach a size of 10 nm, before the width of the QI distribution starts to decrease and the PAC signal of ordered rutile slowly appears. This leads to the conclusion that not only the PAC probes close to the surface layer but also those in the center of the particles experience a disturbed oxygen environment. The initial state of the bare TiO$_2$ nanoparticle is thus characterized by a Ti sublattice with anatase structure and a highly disordered oxygen sublattice.

Details of the oxygen disorder are difficult to infer from the QI distribution. Probably both distributions of the Ti–O distances and bond angles and different numbers of oxygen vacancies contribute. The nanoparticles investigated here had a white to pale yellow color (after synthesis, annealing, and neutron activation). As the color of TiO$_2$ is highly sensitive to the O/Ti ratio,[28] this implies a near-stoichiometric O/Ti ratio $\geq$1.99. Oxygen vacancies must therefore be accompanied by a large number of vacancies in the Ti sublattice. Support for a sizable concentration of such Schottky defects comes from the reduction in density and number of next neighbors found in nanocrystalline γ-Fe$_2$O$_3$ (Ref. 29) and ZrO$_2$.[30] Additionally, Chang and Johnson[31] show that for very small particles a perfect structure is thermodynamically impossible. Their study shows an increasing disorder from the center to the surface of particles.

With increasing temperature, this initial state transforms to a structure giving the PAC signature of coarse-grained rutile. Our data suggest a critical particle size of $d\sim$10 nm for the onset of this process. At this size, first indications of the rutile structure appear in the PAC spectra, independent of the temperature necessary to produce this particle size. In samples I and II of bare n-TiO$_2$, a size of $d\sim$10 nm is

reached at $\sim$500 and $\sim$900 K, respectively (see Fig. 5), and at these temperatures the rutile signal is first seen in the corresponding PAC spectra.

The linewidth δ of the rutile QI decreases with increasing temperature, which can be attributed both to the decrease of the surface fraction by particle growth and to a higher degree of order in the rutile crystallites. The insert in the upper section of Fig. 6 shows that the correlation between the QI linewidth δ and the grain size d is well described by the relation $\delta \propto 1/d$.

The slight difference in the linewidths δ of samples I and II at a given temperature reflects the difference in the particle size. In both samples, the linewidth of coarse-grained TiO$_2$ is reached at particles sizes $d \geq 30$ nm.

After its first appearance at $\sim$500 K, the rutile fraction of sample I remains at a constant level of $\sim$60% up to $\sim$900 K and then increases continuously towards 100% at 1400 K. This two-step behavior possibly reflects the particle size distribution of the sample: A fraction of initially smaller particles reaches the critical size of 10 nm only at 900 K where they start to contribute to the rutile amplitude of the PAC signal. Support for this picture comes from the fact that in sample II with the initially smaller particles, the rutile fraction first appears at a much higher temperature.

The temperature dependence of the QI parameters ν_q and η is illustrated in Fig. 7 using the data of sample I. The quadrupole frequency is practically independent of the thermal history; heating to and cooling from 1400 K produce the same linear trend $\nu_q(T) = \nu_q(0)(1-AT)$ with $\nu_q(0) = 798.9(5)$ MHz and $A = 2.96(7) \times 10^{-5}$ K^{-1}. These values are in fair agreement with those obtained for ^{181}Ta in coarse-grained[13] and single crystal[15] TiO$_2$.

In the case of the asymmetry parameter η, one finds some dependence on the thermal history. In the first heating cycle, the asymmetry parameter of n-TiO$_2$ is slightly smaller than the cg value at the same temperature. Only after reaching 1000–1100 K the temperature dependence of η in n-TiO$_2$ follows the linear trend observed in coarse-grained titania [$\eta(T) = \eta(0)(1-BT)$ with $\eta(0) = 0.547(1)$ and $B = 5.6(1) \times 10^{-5}$ K^{-1}, solid line in the upper section of Fig. 7]. Eastman[24] has reported that annealing at 1073 K is necessary to release the strains present in nonannealed n-TiO$_2$ prepared by gas phase condensation. These strains expand and compress the lattice parameters a and c, respectively. Although we have used a different route of synthesis, strains are to be expected for our samples, too. When these are released by annealing, it is quite likely that the asymmetry parameter is affected. In an *ab initio* calculation Errico *et al.*[32] have recently shown that strength, symmetry, and orientation of the EFG tensor at probe nuclei on the metal site of TiO$_2$ are highly sensitive to the probe charge state and to anisotropic lattice relaxations.

The PAC measurements of the bare particles have established that at a grain size of $d \geq 30$ nm, these particles reach the same degree of order as the coarse-grained material. It is therefore a remarkable observation that the broad frequency distribution in the core of the coated particles, which reflects the disorder of the oxygen sublattice, persists up to 1400 K (see Figs. 8 and 9), where the grain size clearly exceeds the

value of $d \geqslant 30$ nm. In n-Ti(Hf)O$_2$/Al$_2$O$_3$, the rutile PAC pattern appears only at 1450 K, and in n-Ti(Hf)O$_2$/ZrO$_2$ the rutile PAC signal is completely suppressed up to 1400 K. Apparently, the ordering of the anion sublattice in the coated titania kernels is obstructed. The underlying mechanism is not yet clear. One would expect that the mechanical confinement by the coating favors a state of high density with a small number of oxygen vacancies, as has been observed in Al$_2$O$_3$-coated ZrO$_2$ nanoparticles,[16] where the evolution towards well-ordered monoclinic and tetragonal ZrO$_2$ starts as early as $T \sim 500$ K. Possibly, a solid state reaction between the titania kernels and the ZrO$_2$ and Al$_2$O$_3$ coatings plays a role.

V. CONCLUSION

The combination of electron and x-ray diffractions with measurements of electric quadrupole interactions allows complementary insights into structure, phase transition, and grain growth of ceramic nanoparticles. The diffraction methods reflect the degree of long range order of the cation sublattice; the electric quadrupole interaction samples the charge distribution surrounding the metal sites and therefore provides information on the order of the oxygen sublattice. From the results we can sketch a material with a fairly good long range order of the Ti sublattice and a pronounced disorder of the oxygen sublattice, probably caused by oxygen vacancies and distributions of the Ti–O distances and bond angles.

The microwave plasma synthesis of nanocrystalline TiO$_2$ leads to the anatase rather than to the rutile structure, which is usually found in the coarse-grained material. With increasing temperature, grain growth and phase transformations have been observed. Coating the particles with amorphous Al$_2$O$_3$ and crystalline ZrO$_2$, respectively, suppresses the ordering process and phase transformation and also obstructs grain growth.

ACKNOWLEDGMENT

[1] H. Zhang and J. F. Banfield, Chem. Mater. **17**, 3421 (2005).
[2] K.-R. Zhu, M.-S. Zhang, J.-M. Hong, and Z. Yin, Mater. Sci. Eng., A **403**, 87 (2005).
[3] Y. Hu, H.-L. Tsai, and C.-L. Huang, Mater. Sci. Eng., A **344**, 209 (2003).
[4] V. Swamy, A. Kuznetsov, L. S. Dubrovinsky, R. A. Caruso, D. G. Shchukin, and B. C. Muddle, Phys. Rev. B **71**, 184302 (2005).
[5] A. Navrotsky, Geochem. Trans. **4**, 34 (2003).
[6] T. B. Ghosh, S. Dhabal, and A. K. Datta, J. Appl. Phys. **94**, 4577 (2003).
[7] B. Gilbert, H. Zhang, F. Huang, M. P. Finnegan, G. A. Waychunas, and J. Banfield, Geochem. Trans. **4**, 20 (2003).
[8] D. Vollath and K. E. Sickafus, Nanostruct. Mater. **1**, 427 (1992) J. Mater. Res. **8**, 2978 (1993).
[9] D. Vollath and D. V. Szabó, Nanostruct. Mater. **4**, 927 (1994).
[10] D. Vollath and D. V. Szabó, in *Innovative Processing of Films and Nanocrystalline Powders*, edited by K. L. Choy (Imperial College Press, London, 2002).
[11] H. Frauenfelder and R. M. Steffen, in *Perturbed Angular Correlations*, edited by K. Karlsson, E. Matthias, and K. Siegbahn (North Holland, Amsterdam, 1963).
[12] G. Schatz and A. Weidinger, *Nuclear Solid State Physics* (Wiley, New York, 1996).
[13] J. M. Adams and G. L. Catchen, Phys. Rev. B **50**, 1264 (1994).
[14] L. A. Errico, G. Fabricius, M. Renteria, P. de la Presa, and M. Forker, Phys. Rev. Lett. **89**, 055503 (2002).
[15] M. Renteria, G. N. Darriba, L. A. Errico, and P. D. Eversheim (unpublished).
[16] M. Forker, J. Schmidberger, D. V. Szabó, and D. Vollath, Phys. Rev. B **61**, 1014 (2000).
[17] D. Vollath, M. Forker, M. Hagelstein, and D. V. Szabó, Mater. Res. Soc. Symp. Proc. **634**, B7.7.1 (2001).
[18] H. P. Klug and L. E. Alexander, *X-Ray Diffraction Procedures* (Wiley, New York, 1974).
[19] Powder Diffraction File, Joint Committee on Powder Diffraction Standards, JCPDS-ICDD, Card Nos.: 21-1272 (anatase), 21-1276 (rutile), 27-0997 (c-ZrO$_2$), 37-1484 (m-ZrO$_2$), and 42-1468 (corundum).
[20] C. S. Kim, K. Nakaso, B. Xia, K. Okuyama, and M. Shimada, Aerosol Sci. Technol. **39**, 104 (2005).
[21] G. P. Dinda, H. Rösner, and G. Wilde, Solid State Phenom. **101–102**, 55 (2005).
[22] H. Zhang and J. F. Banfield, J. Mater. Chem. **8**, 2073 (1998).
[23] *Fundamentals of Ceramic Powder Processing and Synthesis*, edited by T. A. Ring (Academic, San Diego, 1996).
[24] J. A. Eastman, J. Appl. Phys. **75**, 770 (1994).
[25] M. Forker *et al.*, Nucl. Instrum. Methods Phys. Res. A **327**, 456 (1993).
[26] C. Günther, W. Engels, U. Wehmann, and E. Bodenstedt, Phys. Lett. **10**, 303 (1964).
[27] R. Nitsche, M. Winterer, M. Croft, and H. Hahn, Nucl. Instrum. Methods Phys. Res. B **97**, 127 (1995).
[28] J. C. Parker and R. W. Siegel, Appl. Phys. Lett. **57**, 943 (1990).
[29] E. Pellegrini *et al.*, Phys. Status Solidi B **215**, 797 (1999).
[30] M. Hagelstein, H. O. Moser, D. Vollath, C. Ferrero, and M. Borowski, J. Synchrotron Radiat. **8**, 522 (2001).
[31] J. Chang and E. Johnson, Philos. Mag. **85**, 3617 (2005).
[32] L. A. Errico, G. Fabricius, and M. Renteria, Phys. Status Solidi B **241**, 2394 (2004).